Dynamic stiffness parameter assessment of cracked reinforced concrete beams
A numerical and experimental study

Vandecruys, Eline; Hendriks, Max A.N.; van de Velde, Menno; Lombaert, Geert; Verstrynge, Els

DOI
10.1016/j.engstruct.2024.118758

Publication date
2024

Document Version
Final published version

Published in
Engineering Structures

Engineering Structures 318 (2024) 118758

Contents lists available at ScienceDirect

Engineering Structures

journal homepage: www.elsevier.com/locate/engstruct

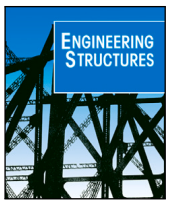

Dynamic stiffness parameter assessment of cracked reinforced concrete beams: A numerical and experimental study

Eline Vandecruys [a,*], Max A.N. Hendriks [b], Menno van de Velde [c], Geert Lombaert [c], Els Verstrynge [a]

[a] Department of Civil Engineering, Materials and Constructions Section, KU Leuven, Kasteelpark Arenberg 40, 3001 Leuven, Belgium
[b] Faculty of Civil Engineering and Geosciences, Concrete Structures Section, TU Delft, Stevinweg 1, 2628 CN Delft, The Netherlands
[c] Department of Civil Engineering, Structural Mechanics Section, KU Leuven, Kasteelpark Arenberg 40, 3001 Leuven, Belgium

ARTICLE INFO

Keywords:
Concrete cracking
Structural stiffness
Reinforced concrete
Rebar corrosion
Dynamic testing

ABSTRACT

A major challenge of infrastructure management is to predict the remaining capacity of degrading structures and safely prolong their lifetime. In reinforced concrete (RC) structures, concrete cracking has a significant effect on durability and stiffness properties. Structural integrity degradation is often assessed by estimating the global stiffness loss through vibration-based structural health monitoring. Yet, this is challenging as the modal characteristics might also be affected by environmental and support conditions. At the same time, the development of models that enable studying the modal characteristics of cracked concrete structures has received little attention so far. This paper proposes a novel, visual inspection-based method to predict the decrease in effective elastic moduli of existing concrete structures from observed longitudinal and transverse cracks which are typical for corrosion and load-induced damage in RC elements. Discrete and smeared finite element models are developed to establish a relation between the geometrical crack properties and the changes in the concrete's smeared dynamic stiffness parameters, as defined within an orthotropic material model. It is found that the crack pattern has a significant influence, with transverse cracks generally reducing the stiffness parameters more than longitudinal cracks. Experimental data support the proposed relations' ability to tune the parameters of the orthotropic material model based on crack properties from corroded or mechanically loaded RC beams. The proposed relations enhance the assessment of serviceability limit states in RC beams and offer a valuable tool to evaluate dynamic test data obtained from on-site monitoring.

1. Introduction

Damage assessment in existing reinforced concrete (RC) structures is a major concern in infrastructure maintenance. In recent years, an increase in the number of structures with significant signs of deterioration is noticed due to ageing of the structures and growing traffic volumes. Reinforcement corrosion and load-induced cracking are frequently occurring damage mechanisms, resulting in longitudinal and transverse cracks of the RC elements. These cracks highly influence the durability [1] and serviceability [2] of the degraded structure and should be assessed thoroughly to estimate the risk of structural failure.

In order to quantify the structural effect of concrete cracking and predict the remaining capacity of a structure, damage identification methods based on vibration-based structural health monitoring (SHM) have been extensively investigated [3,4]. Dynamic testing of damaged RC elements has shown to be a challenging yet promising assessment method [5]. On site, vibration-based SHM is often used when assessing structures on a global scale, since the results provide information about the changes in stiffness and structural integrity [6–8] as well as remaining service life [9]. When concrete cracks, the structural stiffness is affected which in turn influences the modal characteristics of a structure (e.g. natural frequencies, mode shapes and modal damping). In model-based SHM, the measured modal characteristics are compared to those obtained during analysis of a finite element (FE) model [10] to calibrate the model and predict the stiffness change and performance of the structure [9,11]. The developed finite element model is deemed accurate when the results of the modelled and measured modal characteristics correspond well, which can be obtained through updating of the stiffness-related parameters of the structural elements and the support conditions [11–13].

Even though modal characteristics provide valuable information on the global stiffness, dynamic testing is complex as reference data for the undamaged structure are often lacking and the results also depend on

* Corresponding author.
E-mail address: eline.vandecruys@kuleuven.be (E. Vandecruys).

https://doi.org/10.1016/j.engstruct.2024.118758
Received 17 April 2024; Received in revised form 9 July 2024; Accepted 6 August 2024
Available online 16 August 2024

environmental and support conditions [14]. Besides dynamic testing, complementary numerical and inspection-based approaches have been investigated in the literature to assess degraded structures. Until now, most research on the effect of degradation on the structural behaviour of RC has been focussed on rebar corrosion damage. Many theoretical and empirical relations are developed to obtain realistic material properties and damage models for corroded structures [15,16], with the aim of establishing realistic FE representations of the damaged structure and predict its remaining capacity. Yet, comprehensive approaches on how to account for the stiffness effect of observed crack formation in FE models are lacking and this issue remains an important area of investigation.

A first method to model the development of corrosion cracks has been established by simulating the expansion of corrosion products and increasing the internal pressure around the rebar. This process causes concrete cracking, which has shown promising results in accurately modelling the occurrence of corrosion cracks [17,18]. However, such detailed approach is difficult to upscale to real-life structures. Second, the remaining strength of the cracked concrete can be reduced in order to simulate concrete cracking based on measured tensile strains [15], corrosion levels [19] or ultrasonic pulse velocities (UPV) [20]. A much applied relation between the remaining compressive concrete strength (f_c^*) and apparent tensile strains was developed by Coronelli and Gambarova [15] (Eq. (1)), based on the model by Vecchio and Collins [21].

$$f_c^* = \frac{f_c}{1 + K\varepsilon_1/\varepsilon_{co}} \tag{1}$$

In Eq. (1), f_c is the initial compressive concrete strength, K is a coefficient related to bar roughness and diameter, ε_1 is the average smeared tensile strain in the cracked concrete and ε_{co} is the strain at the peak compressive stress. The relation is valid when cracks develop in a direction which is parallel to the applied compression loads and was established after performing shear and compression tests on squared RC panels [21]. Hence, Eq. (1) is developed for in-plane stress states. Furthermore, the relation is not adaptable to different crack directions and does not consider the amount of cracks, therefore lacking versatility.

In addition to reducing the concrete strength, concrete cracking also influences the structural stiffness [22,23]. The effect of cracking on the effective elastic modulus of the concrete can be determined by relating the stiffness to the reduced strength of cracked concrete [16,24]. However, this methodology implies the same limitations as noticed for f_c^*, since it does not take into account the actual crack pattern. Alternatively, an attempt at directly relating the stiffness decrease to the corrosion level has been made by Torres-Acosta et al. [25] through empirical relations based on elaborate experimental testing. Yet, empirical relations are often only applicable for the considered set-up. It can be concluded that, even though various methods to model stiffness decreases in corroded structures were developed, they do not take into account the actual crack patterns, although these significantly affect the material properties [26]. The compressive strength and stiffness have shown to be strongly influenced by crack widths and their directions [27], but this aspect has remained underexplored in the literature, thus leaving room for further advancements in relating crack patterns to concrete stiffness degradation.

In finite element (FE) models, concrete cracking can either be modelled by smeared cracking or discrete cracking approaches. The smeared cracking methods consider a cracked material as a continuum, while the discrete cracking methods represent a crack as a geometrical discontinuity. The smeared cracking method has been developed in the 1980s to facilitate linear analysis of cracked materials [28–30]. The method consists of reducing the effective elastic modulus or strength of the material in the zone where damage occurs [31,32], which generally requires less detailed information about the crack pattern and is more convenient for updating a finite element model of the structure based on modal characteristics. Therefore, model-based SHM strategies often use the smeared cracking approach and model concrete cracking as a decrease in strength and effective elastic modulus of the damaged concrete [9,16]. On the other hand, the cracks can also be represented in an FE model through discrete cracking, where individual cracks are modelled separately. This approach offers a more realistic representation of the damaged structure since the direction and location of a crack can be implemented explicitly. Pre-existing cracks can either be modelled through a weakened-element approach in case of small mesh sizes, or by introducing interfaces in the FE model [33,34].

The present study aims at developing a relation between the crack pattern caused by deterioration of RC beams and the decrease in stiffness parameters of discrete and smeared crack models, allowing to assess, numerically, the changes in modal characteristic. The key novelty of this research is evaluating the direct link between the observed multi-directional geometrical crack data and the material parameters of the smeared and discrete crack models by comparing the effect at structural level with dynamic test data. The geometrical crack data, containing valuable information on deterioration, are not considered in most of the existing methodologies that relate cracking to stiffness decreases [15,19,20,35], even though the crack parameters have proven critical in evaluating the material's stiffness loss [26,27]. Moreover, an orthotropic concrete material model is introduced in order to differentiate between longitudinal and transverse cracking in smeared crack FE models.

The structure of the paper is as follows: In Section 2, an experimental programme is described where natural frequencies are obtained during corrosion and four-point bending tests of RC beams. The tests were executed by the authors and summarised here to provide data for validation of the developed relations. Section 3 discusses the development of an accurate 3D FE model for dynamic analysis of undamaged RC beams, which is calibrated to fit the output of the undamaged tested beams. Section 4 describes an approach to include discrete cracks with degraded crack properties in the FE model (Fig. 1a). Aim of the detailed discrete crack model is to determine the beams' modal characteristics, based on various crack patterns. In Section 5, a smeared cracking approach is implemented with reduced orthotropic stiffness properties (Fig. 1b). This model links the stiffness properties of the degraded zone in the beams to their modal characteristics. Finally, Section 6 relates discrete and smeared crack models with similar modal characteristics in order to obtain a relation between the crack parameters and stiffness loss. To evaluate the findings, the developed relations are validated with experimental test data.

2. Experimental test programme

To validate the relations between crack parameters and stiffness, the modal characteristics of four beams tested as part of an elaborate experimental test programme at KU Leuven [36,37] are considered. The four beams were subjected to two damage mechanisms, including accelerated corrosion and mechanical loading. The beams had dimensions 150 × 200 × 2000 mm^3 and contained both longitudinal rebars and stirrups, as illustrated in Fig. 2. The first step of the experimental test programme consisted of an accelerated corrosion process of 18 weeks, with an impressed current density of 100 μA/cm^2. The tensile reinforcement of beams L_{sym} and L_{asym} was corroded over a local area of 400 mm while the tensile reinforcement of beam U was uniformly corroded over its entire length, as illustrated in Fig. 2b. A detailed description of this corrosion process can be found in [36]. During corrosion, crack measurements were performed every two weeks and dynamic tests were performed every four weeks. The beams developed many longitudinal cracks at their bottom surface (Figs. 3a, 3c, 3e and 4a), and weighing of the rebars at the end of the test programme showed rebar mass losses of around 11% (Table 1). The fourth sample, beam R, acted as a reference beam which was not subjected to corrosion.

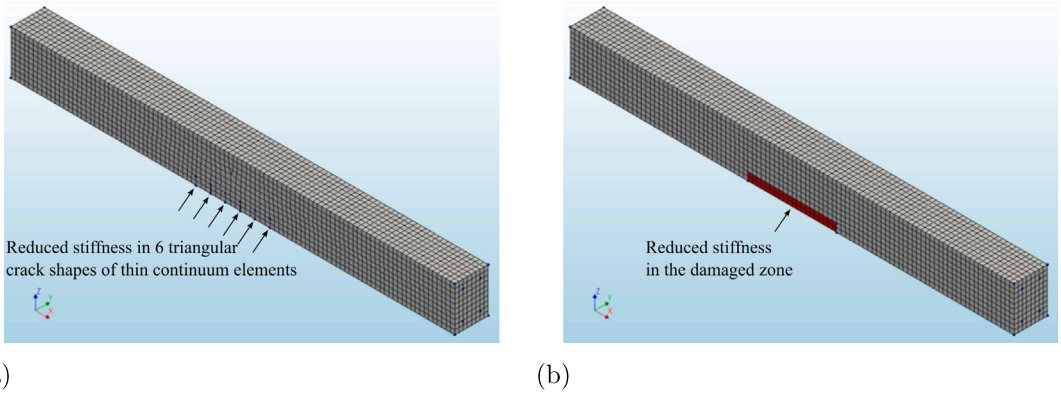

Fig. 1. Illustration of the (a) discrete crack model with weakened element approach for crack representation and (b) smeared crack model with reduced stiffness in the damaged zone, modelled in DIANA.

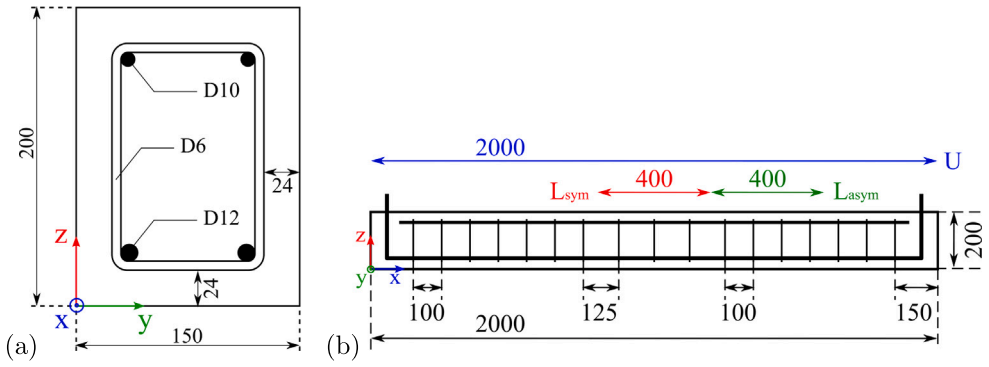

Fig. 2. (a) Cross-section and (b) longitudinal reinforcement layout of the RC beams with indication of the corrosion zones in blue (U), red (L_{sym}) and green (L_{asym}). Dimensions in mm. (For interpretation of the references to colour in this figure legend, the reader is referred to the web version of this article.)
Source: Figure adapted from [36].

Table 1
Overview of the tested beams, their average corrosion level of the corroded length, and yielding load.

Beam	Corrosion level [%]	Yielding load [kN]
R	0	57.41
U	10.77	47.86
L_{sym}	11.93	50.60
L_{asym}	12.02	50.42

After the corrosion period, all four beams were subjected to progressive cyclic four-point bending with load steps of 12 kN, 6 kN per loading pin, as discussed in detail in [37]. During the flexural tests, the beams were monitored through crack measurements (Figs. 3b, 3d, 3f and 4b) and dynamic testing after every load cycle, with the exception of beam U. Eventually, the beams failed at total loads between 48 and 58 kN, due to yielding of the rebars (Table 1). Since beam U was corroded over its entire length, this beam had the lowest remaining capacity. Beams L_{sym} and L_{asym} also showed reduced yielding loads in comparison to the reference beam due to their local corroded areas that were (partly) positioned in the region of constant bending moment.

3. Uncracked FE model

As a first step in developing discrete and smeared crack models of the tested beams, an uncracked 3D FE model is created in the DIANA software which acts as a basis for further cracked beam models. The concrete part of the beams is modelled as an elastic solid while the longitudinal reinforcement is modelled by truss elements. The model is constructed using a quadrangle mesher type and using quadratic elements, with a mesh size of 20 mm. In order to obtain free vibration modes, free-free boundary conditions are considered when solving the structural eigenvalue analysis. The geometry of the uncracked RC model is created based on the dimensions of the experimentally tested beams (Fig. 2).

The concrete's static Young's modulus is derived from the compressive strength, as outlined in the Eurocode [38]. However, it should be noted that this estimation of the Young's modulus is prone to large uncertainties, as research has shown that the Young's modulus not only depends on the compressive strength, but also on properties of the concrete mix such as the material density [39] and nature of the aggregates [40], and on cross-section properties [40]. Nevertheless, this research focusses on the beam's dynamic stiffness, which is determined further in this chapter by minimising the root mean squared error (RMSE) between the measured and simulated natural frequencies, without relying on an initial estimation of the concrete's static stiffness. The concrete compressive strength and mass density are calculated based on standard experimental tests according to European standards [41,42], resulting in f_{cm} = 49.5 MPa and ρ_c = 2377 kg/m^3, respectively. Furthermore, the concrete's Poisson's ratio as well as the material properties of the reinforcing steel are determined based on standard values reported in the Eurocode [38,43]. An overview of all material properties used as inputs for the FE model can be found in Table 2. For now, isotropy is assumed and the shear mode can therefore be determined by Eq. (2).

$$G = \frac{E}{2 \cdot (1 + \nu)} \tag{2}$$

In this study, the concrete and steel are assumed linear elastic since the purpose of the developed approach is to assess the serviceability limit states in reinforced concrete beams under typical loading conditions and evaluate dynamic test data. Both applications do not require non-linear FE analysis due to the small deformations involved.

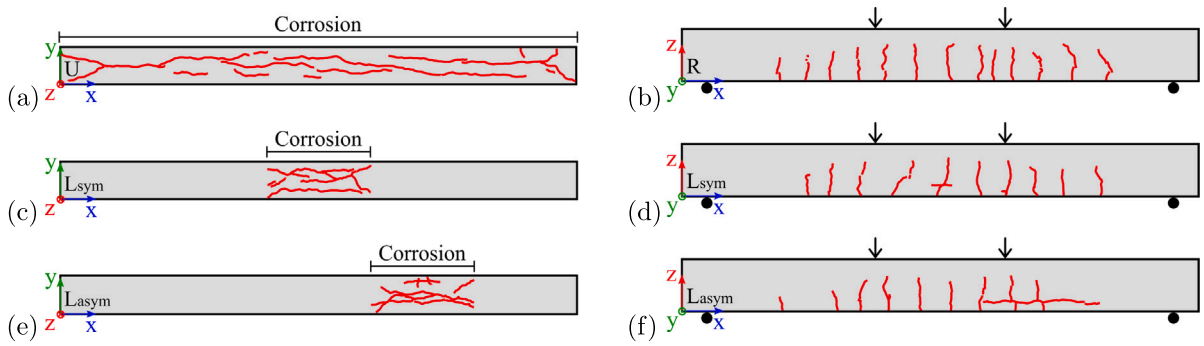

Fig. 3. (a, c, e) Crack patterns of the beams after corrosion, in bottom view, with indication of the corrosion zone. (b, d, f) Crack patterns of the mechanically loaded beams after sustaining a 48 kN load during four-point bending, in side view.

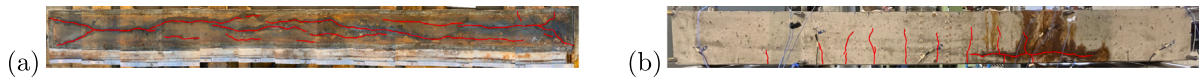

Fig. 4. Pictures of the crack patterns (a) after corrosion of beam U in bottom view and (b) after sustaining a 48 kN load during four-point bending of beam L_{asym} in side view.

Table 2
Material properties as implemented in the FE model. The darker the symbol shade, the larger the influence on the dynamic output.

Property	Symbol	Value	Unit	Methodology
		Concrete		
Young's modulus	E_c	35.5	GPa	$E_c = 22(f_{cm}/10)^{0.3}$ [38]
Poisson's ratio	ν_c	0.2	-	Standard value [38]
Mass density	ρ_c	2377	kg/m^3	Weighing of cubes [42]
		Steel		
Young's modulus	E_s	200	GPa	Standard value [38]
Poisson's ratio	ν_s	0.3	-	Standard value [43]
Mass density	ρ_s	7850	kg/m^3	Standard value [38]

Table 3
Natural frequencies (B: vertical bending modes, L: lateral bending modes and T: torsional modes) of the measured (DT) and modelled (FE) uncracked beams. The measurements are averaged over four beams, and their standard deviation (σ_{DT}) is shown between brackets. The last column presents the relative change between the measured and modelled natural frequencies.

Mode	f_{DT} (σ_{DT}) [Hz]	f_{FE} [Hz]	Δf_n [%]
B1	210.0 (1.7)	210.0	−0.0
B2	549.2 (4.6)	546.1	+0.56
B3	994.4 (7.5)	995.6	−0.12
L1	154.4 (1.0)	158.0	−2.33
L2	415.3 (5.4)	420.6	−1.28
L3	787.8 (5.6)	787.6	+0.03
T1	602.7 (2.3)	580.1	+3.75
T2	1152.5 (8.0)	1160.0	−0.65

The material parameters which influence the modal characteristics the most are highlighted in Table 2. The darker the shade of the second column, the larger the influence on the modal characteristics, as tested by an exploratory numerical study. The influential parameters include the Young's modulus, Poisson's ratio and mass density of the concrete and steel. In addition, since the volume of concrete material is larger than the volume of reinforcement steel, the material parameters of concrete have a larger effect on the modal characteristics.

In order to obtain a good match between the simulated and measured modal characteristics, the FE model is calibrated. As our previous research showed that natural frequencies (f_n) are a reliable modal characteristic for damage assessment [5], this paper exclusively focusses on the simulated and measured natural frequencies. Moreover, the first three bending modes (B1, B2 and B3), three lateral modes (L1, L2 and L3) and two torsional modes (T1 and T2) are considered. Since the natural frequencies of the uncracked FE model are most affected by the concrete mass and stiffness, and the concrete mass has been accurately measured, the concrete stiffness is adapted to reach a minimal RMSE between the measured and modelled natural frequencies, as presented in Eq. (3).

$$\text{RMSE} = \sqrt{\frac{\sum_{i=1}^{N} (f_{DT,i} - f_{FE,i})^2}{N}} \tag{3}$$

In this equation, $f_{DT,i}$ are the measured natural frequencies obtained during dynamic testing (DT), and $f_{FE,i}$ are the modelled natural frequencies for all eight considered modes ($N = 8$). The minimal RMSE is reached for a dynamic concrete stiffness of $E_{c,dyn} = 41.2$ GPa. This value is 1.16 times larger than the initially estimated static concrete stiffness of $E_c = 35.5$ GPa (Table 2). Even though the initial static concrete stiffness may contain uncertainties due to the employed relation of the Eurocode [38], an increase in dynamic stiffness in comparison to the static stiffness is generally accepted in the literature [44]. The natural frequencies of the resulting calibrated uncracked beam model are presented in Table 3 and compared to the mean experimental outputs of the four tested beams as recorded before the start of the corrosion process.

4. Discrete crack model

The purpose of the discrete crack model is to accurately replicate cracked beams by incorporating the actual crack properties in the 3D FE model. Pre-existing cracks are explicitly modelled in a discrete crack model through either incorporation of interfaces or by assigning weakened properties to the elements inside the cracks [33]. After preliminary testing, it was found that both methods generate the exact same dynamic output when similar crack parameters were chosen. Given the simplicity of the weakened element approach, it was opted to use this approach.

4.1. Weakened elements approach

The discrete crack model of the damaged beams is developed by integrating triangular crack shapes into the beam geometry. After meshing, the elements inside the crack are assigned weakened material properties. Besides from the incorporation of cracks, the discrete crack model is identical to the model described in Section 3. To accurately reproduce the actual crack patterns, the crack dimensions are based on measured crack widths, locations and depths. Further, the weakened material inside the cracks is assumed to behave linear-elastic.

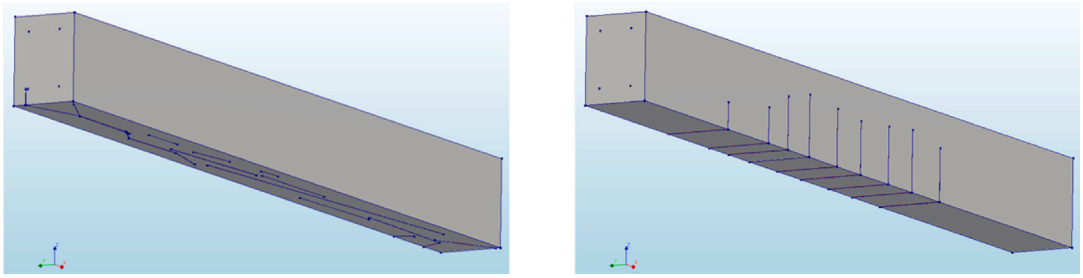

(a) (b)

Fig. 5. Illustration of the discrete crack models to represent (a) beam U at the end of corrosion and (b) beam L_{asym} after sustaining a load of 48 kN.

The corresponding material properties are determined by fitting the predicted and measured natural frequencies of the cracked beams. Similar to the concrete material properties described in Section 3, the cracks' material properties which affect the modal characteristics are the Young's modulus, Poisson's ratio and mass density. As the Poisson's ratio of cracked concrete can be taken equal to zero [38] and also the mass density inside the crack is assumed to be almost zero, the only relevant material property which requires optimisation through comparison with experiments is the Young's modulus of the material inside the crack.

To compare the discrete crack FE models to the corroded and mechanically tested beams, the measured crack patterns of the damaged beams are replicated in the FE model. The representative FE models replicating beam U at the end of corrosion and beam L_{asym} after sustaining a load of 48 kN are presented in Fig. 5. Similar models are made for all four beams at various damage levels, i.e. at several stages of the corrosion process and with increasing load steps during the bending process. During accelerated corrosion, each time a dynamic test was performed, also the crack pattern was measured and can hence be implemented in an FE model. Due to practical limitations, dynamic tests during cyclic four-point bending could only be performed in unloaded conditions. The crack widths, however, were measured under loaded conditions since this facilitates the measurements and provides the most representative data for on-site inspections.

Fig. 6 shows results obtained during four-point bending of uncorroded beam R, where the measured evolution of the natural frequencies is compared to the one predicted by an FE model with crack patterns as observed during experimental bending tests. Moreover, the predicted results for different values of the Young's modulus of the crack material (E_w) are compared to find the one which leads to the best match. Optimisation of E_w is performed by minimising the RMSE, which was presented in Eq. (3). However, $f_{DT,i}$ and $f_{FE,i}$ are now replaced by $\Delta f_{DT,i}$ and $\Delta f_{FE,i}$, respectively, to represent the relative changes in natural frequencies in comparison to the beam's undamaged condition. Comparison between FE models with different crack stiffnesses shows that the RMSE with E_w = 20 MPa is the smallest ($RMSE_{10\ MPa}$ = 4.39%, $RMSE_{20\ MPa}$ = 2.60%, $RMSE_{40\ MPa}$ = 3.62%) when all eight considered modes and five loading steps are taken into account (N = 40). Therefore, the stiffness inside the cracks is reduced to E_w = 20 MPa in order to reach agreement between the predicted and measured evolutions in natural frequencies for all modes. This crack stiffness is 2060 times smaller compared to the dynamic stiffness of the surrounding undamaged concrete ($E_{c,dyn}$ = 41.2 GPa).

Since the crack stiffness of E_w = 20 MPa is only calibrated based on the four-point bending results of one beam (R), further validation of the discrete crack model is required. As discussed in Section 2, three beams were corroded across different zones, and dynamic and crack measurements were performed during the corrosion process. In addition, all beams with the exception of beam U were also monitored during four-point bending. The measured crack patterns and corresponding natural frequencies are used for validation of the discrete crack model and calibrated crack stiffness. Figs. 7 and 8 present the relative difference in identified natural frequencies of all experimentally cracked beams in comparison to their respective discrete crack FE models during corrosion and four-point bending, respectively.

The experimental results from corrosion of beams U, L_{sym} and L_{asym} in Fig. 7 show that the corrosion cracks have a negligible influence on the vertical and lateral bending modes, as the decrease in natural frequencies only reaches around −3%. Since such small relative decreases could also be linked to creep and shrinkage of the tested beams, it can be questioned whether this natural frequency decrease is indeed caused by the corrosion damage [36]. Therefore, a 95% confidence interval (CI) is indicated in Fig. 7 to illustrate the measurement uncertainties, based on the fluctuations in natural frequencies of uncorroding reference beams. More detailed information about the methodology which was used to obtain the CI can be found in [36]. The measured bending and lateral modes mostly fall within this CI, and can therefore not clearly be attributed to corrosion. The torsional modes, however, are significantly influenced by corrosion cracks, as these changes in natural frequencies reach up to −6% for the uniformly corroded beam, and reach outside of the 95% CI. Despite this clear decrease for T1 and T2 for beam U, the locally corroded beams show less pronounced decreases due to the limited extent of the damaged zone. The difference between frequency changes of the bending, lateral and torsional modes can be explained by the direction of the cracks, as was also reported in the literature [36,45]. Since primarily the longitudinal rebars are corroded in this experimental programme, the corrosion cracks develop in a longitudinal direction, causing very small effects on bending and lateral modes, and larger decreases in natural frequencies of torsional modes.

The simulated results of the FE beam models with corrosion cracking present similar findings, as again the torsional modes show the largest decreases in natural frequencies, while the bending and lateral modes show an insignificant decrease. When only taking into account the results of T1 and T2, the RMSE of the relative natural frequency decrease over all three beams during the corrosion process equals 1.94%. Given that the relative decrease in natural frequencies for torsional modes reaches up to −6%, this value indicates a good agreement between experiment and model for the previously determined crack stiffness of 20 MPa. Even though this crack stiffness was calibrated based on cracking during four-point bending tests, it also yields accurate results for corrosion cracking.

During four-point bending, the natural frequencies are expected to decrease more significantly than during corrosion, due to the overall larger cracks and their transverse direction. This is confirmed by the measurements shown in Fig. 8. Moreover, natural frequencies decrease most for the vertical bending modes, up to −20%, which can be explained by the transverse direction of the bending cracks. Natural frequencies of torsional modes are influenced the least by this transverse crack pattern. Due to the large difference in relative changes of natural frequencies between corrosion and bending cracks, corrosion cracks will not be considered in this research during assessment of

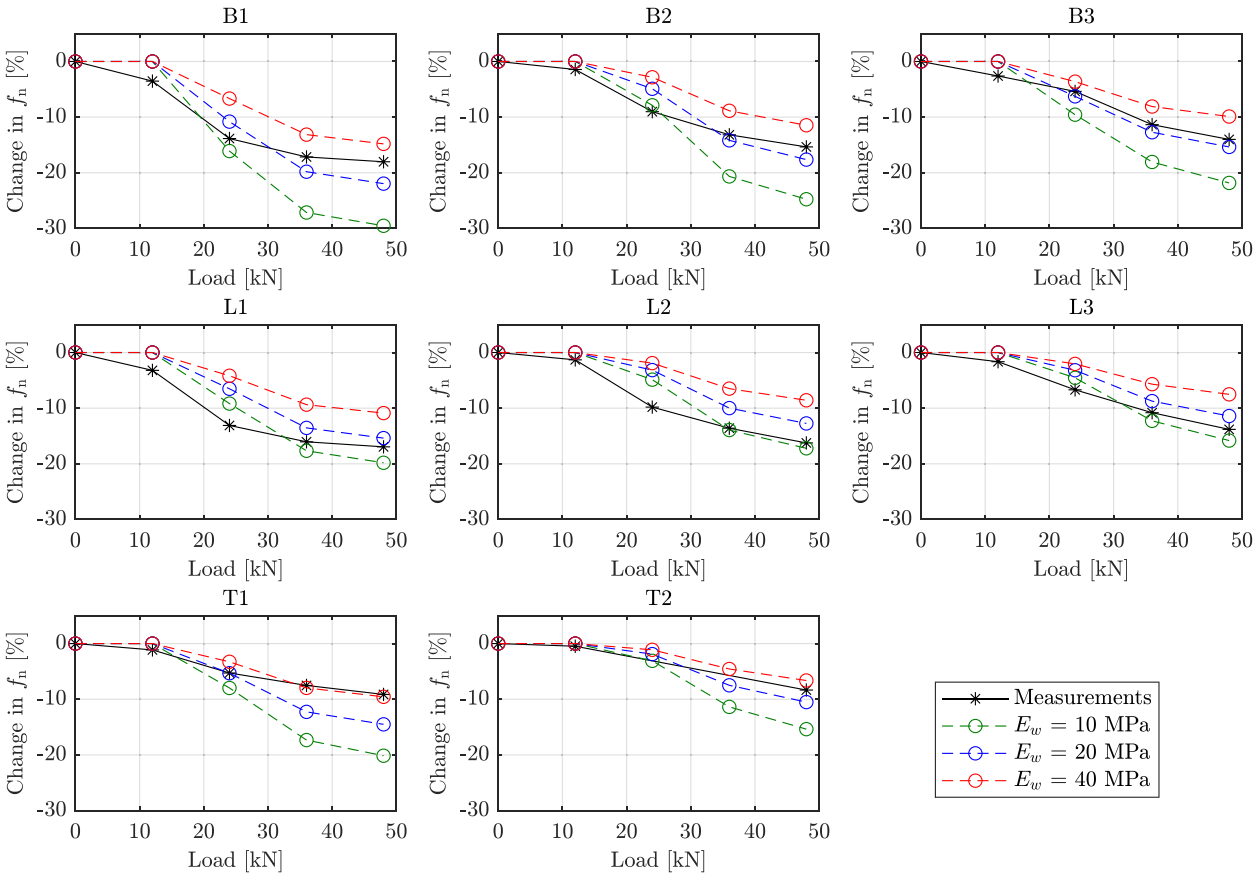

Fig. 6. Relative changes in natural frequencies during bending of beam R, compared to modelled results with different crack stiffnesses as a function of load level. Each graph represents a different mode.

the structural stiffness for cases where also severe bending cracks are present.

Fig. 8 shows that the modelled and measured natural frequency decreases align well during four-point bending, with an overall RMSE of only 2.83% for the different modes and subsequent loading steps. Since the decreases in natural frequencies during bending reach up to −20%, the RMSE confirms that the discrete crack model accurately simulates the modal characteristics of the cracked beams when a crack stiffness of 20 MPa is used.

4.2. Sensitivity of the modal characteristics on crack properties

The calibrated models are subsequently used for sensitivity studies. As shown by the experimental results in Figs. 7 and 8, the crack orientation has a large effect on the dynamic output. Therefore, the influence of longitudinal corrosion cracks and transverse bending cracks on the modal characteristics is discussed separately.

4.2.1. Longitudinal cracking

First, the crack properties need to be defined. These properties include the crack width ($w_{c,l}$) and number of longitudinal cracks ($N_{c,l}$) within the damaged zone, where the l stands for longitudinal. The crack width is presented by the average apparent tensile strain (ε_l) over the beam width (b [mm]):

$$\varepsilon_l = \frac{\sum w_{c,l}}{b} \text{ [−]} \tag{4}$$

Further, the normalised number of cracks over the beam width (N_l) is presented by Eq. (5):

$$N_l = \frac{N_{c,l}}{b} \cdot 1000 \text{ [1/m]} \tag{5}$$

The model results in Fig. 9 show the effect of the normalised crack width and number of cracks on the relative change in natural frequencies f_n for 2000 [mm] long beams with corrosion damage between 400 mm and 1600 mm over their length. The depth of the modelled cracks is set equal to the concrete cover, as corrosion cracking initiates at the rebar surface, and only cracks in the direction of the smallest cover depth are considered (i.e. only on the beam's bottom surface). Fig. 9a shows that, when the number of cracks is kept constant, natural frequencies decrease with increasing apparent tensile strain (ε_l) or crack width. Similarly, Fig. 9b shows a decrease in natural frequencies with increasing amount of cracks when the apparent tensile strain remains constant. The chosen constant values for N_l = 33.3/m in Fig. 9a and ε_l = 0.01 in Fig. 9b are deliberately set to facilitate the comparison of the results with highest x-value in both graphs. The decreasing rate of both graphs seems to diminish when large values of ε_l and N_l are reached, as the other crack parameter remains constant. The presented changes in natural frequencies f_n are most pronounced for the torsional modes and slightly noticeable for lateral modes. This agrees with the observations that were made in the experimental results of Fig. 7, where corrosion cracking mainly influenced torsional modes.

4.2.2. Transverse cracking

Similar to the longitudinal cracks, the effect of crack width and number of cracks on the modal characteristics is investigated for transverse cracking. These parameters are both normalised over a certain section length (l_s). In this study, a section length of 400 mm is chosen, as this length is proportional to the length scale of the damage that would be expected in beams with the considered geometry. One such section is illustrated in the smeared crack model of Fig. 1b. The apparent average tensile strain (ε_t) is defined based on the crack widths ($w_{c,t}$), where t

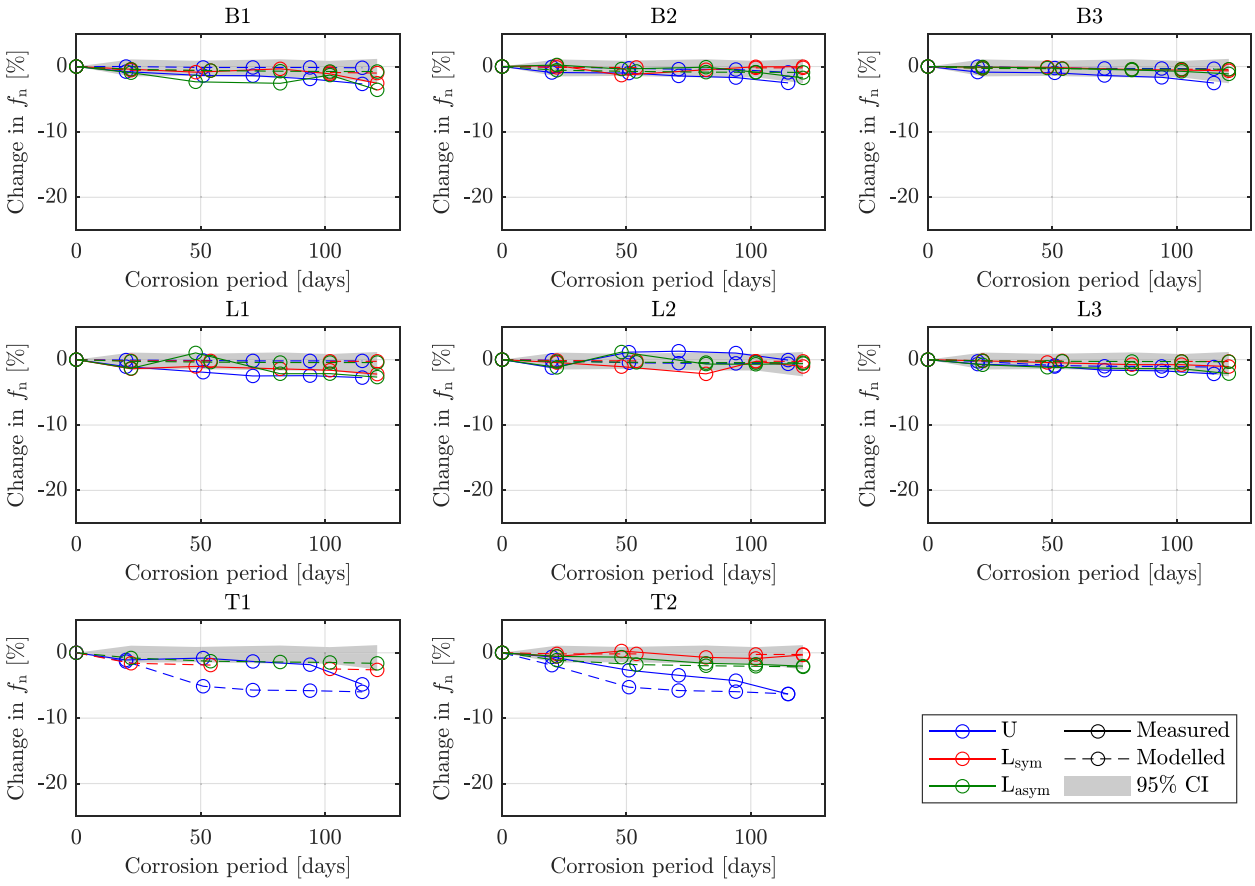

Fig. 7. Relative changes in measured natural frequencies during corrosion of beams U, L_{sym} and L_{asym} (full lines) compared to the simulations with the discrete crack models (striped lines) as a function of the corrosion level. Each graph represents a different mode.

represents transverse cracking, and the section length (l_s [mm]):

$$\varepsilon_t = \frac{\sum w_{c,t}}{l_s} \text{ [−]} \tag{6}$$

The normalised number of transverse cracks (N_t) is similarly calculated by Eq. (7) based on the absolute number of cracks ($N_{c,t}$) divided by the section length:

$$N_t = \frac{N_{c,t}}{l_s} \cdot 1000 \text{ [1/m]} \tag{7}$$

The modelled effect of the transverse number of cracks and the crack width is illustrated in Fig. 10. Again, the damage is induced between 400 mm and 1600 mm along the length of a 2000 mm beam, and the depth of the cracks is taken equal to the concrete cover. For Fig. 10a, the amount of cracks is set to $N_t = 32.5$ cracks/m, while Fig. 10b presents results when $\varepsilon_t = 0.01$. These values are chosen to facilitate the comparison of the results with highest x-value in both graphs, as well as the comparison with Fig. 9. The results clearly show a decrease in natural frequencies with increasing tensile strain or amount of cracks. However, the rate of natural frequency decrease diminishes for large values of ε_t when N_t is kept constant, and vice versa. As expected, the maximum decrease in natural frequencies is much more pronounced for transverse cracks than for longitudinal cracks, as seen by comparison of Figs. 9 and 10.

5. Smeared crack model

A smeared crack model is developed in order to obtain a relation between the stiffness decrease of the damaged zone and the modal characteristics of the beam. The smeared crack models cannot be calibrated with geometrical crack data as the cracks are modelled indirectly by a reduced stiffness. Instead, in Section 6, the modal characteristics of the developed smeared crack model will be compared to the modal characteristics of the discrete crack models.

5.1. Orthotropic material properties

As discussed before, concrete cracks can be modelled as a decrease in concrete stiffness of the damaged zone. However, an isotropic decrease of $E_{c,dyn}$ would not be able to differentiate between longitudinal and transverse cracks. Therefore, a linear elastic orthotropic concrete material is introduced for the cracked concrete within the damaged zone. This damaged zone is restricted by the measured crack depth and the crack location along the beam's x-axis, as illustrated in Fig. 1b. Meanwhile, the mass density of the damaged concrete remains equal to $\rho_c = 2377$ kg/m^3, as determined in Section 3. The orthotropic material model is able to alter the Young's modulus, Poisson's ratio and shear modulus of the cracked zone in all three dimensions separately. As the Poisson's ratios have little to no influence on the modal characteristics, they are not considered here as independent variables. The directions with regards to the beam geometry are shown in Fig. 2, with the x-axis positioned along the beam length, y-axis for the depth, and z-axis for the height. The Young's moduli and shear moduli all have different impacts on the different dynamic modes, as numerically tested and illustrated in Table 4. $E_{c,y}$, $E_{c,z}$ and $G_{c,yz}$ do not influence the modal characteristics of the beam, as is also assumed by the Euler–Bernoulli beam theory. Moreover, $E_{c,x}$ does not affect the torsional modes, as torsion does not induce normal strain deformations in the x-direction. Vertical bending and lateral modes cause shear deformations in the xz and xy plane, respectively, and torsional modes cause shear deformations in both xz and xy planes. This explains the influence of $G_{c,xz}$ and $G_{c,xy}$ on the modal characteristics as presented in Table 4.

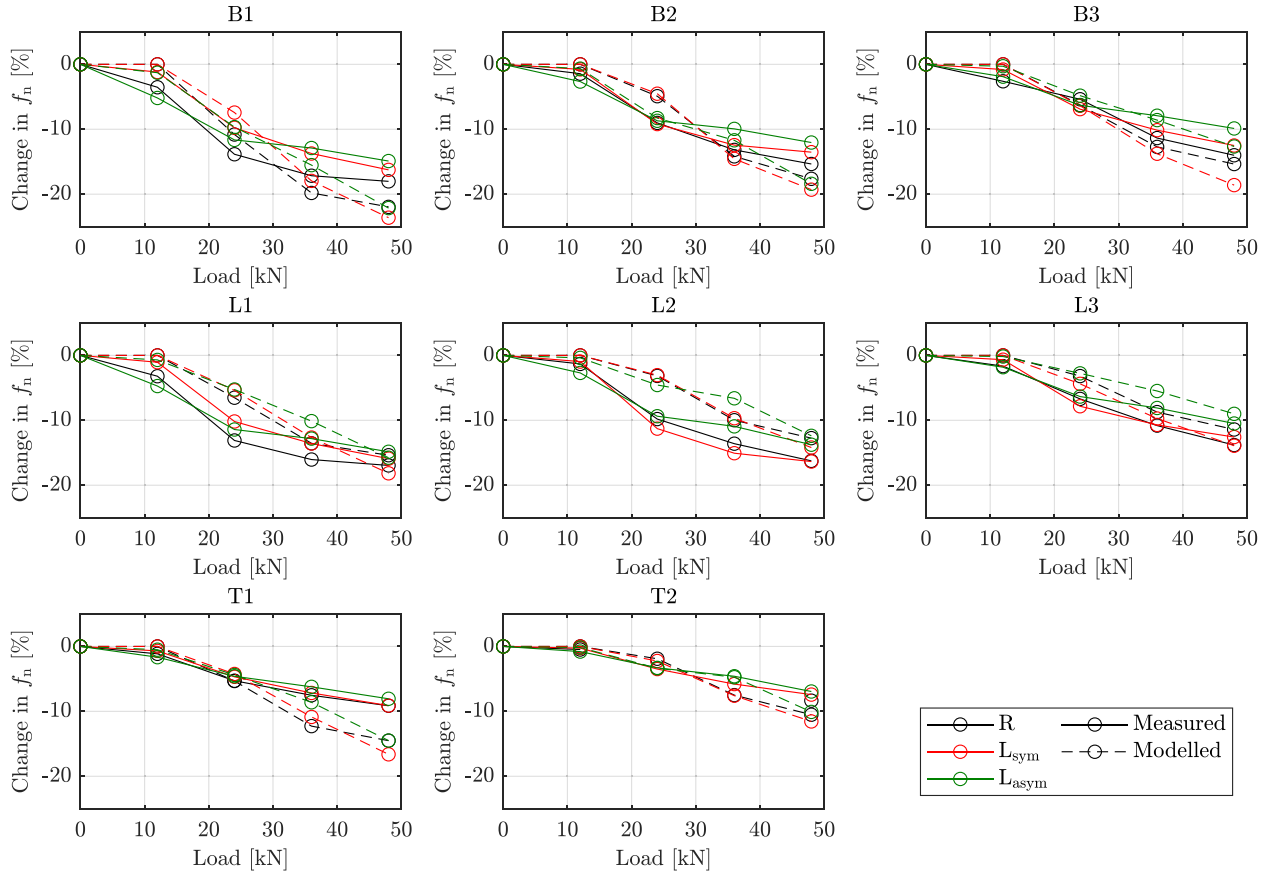

Fig. 8. Relative changes in measured natural frequencies during mechanical bending of beams R, L_{sym} and L_{asym} (full lines) compared to the simulations with the discrete crack models (striped lines) as a function of the load level. Each graph represents a different mode.

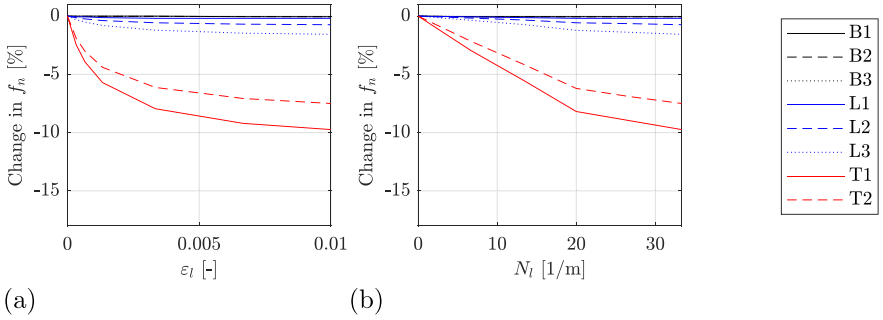

Fig. 9. Influence of (a) ε_l (with constant $N_l = 33.3$/m or 5 cracks over the beam width) and (b) N_l (with constant $\varepsilon_l = 0.01$) on the natural frequencies of a beam with longitudinal cracks.

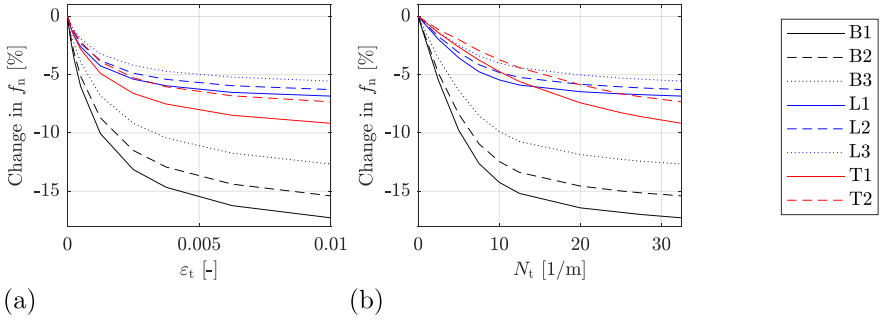

Fig. 10. Influence of (a) ε_t (with constant $N_t = 32.5$/m or 13 cracks over the section length) and (b) N_t (with constant $\varepsilon_t = 0.01$) on the natural frequencies of a beam with transverse cracks.

Table 4
Influence of the different orthotropic concrete material properties on the bending (B), lateral (L) and torsional (T) modes. The x, y and z-direction are illustrated in Fig. 2.

	$E_{c,x}$	$E_{c,y}$	$E_{c,z}$	$G_{c,xy}$	$G_{c,yz}$	$G_{c,xz}$
B	■					■
L	■			■		
T						■

Theoretically, perfectly longitudinal corrosion cracks along the bottom of the beam will only have an influence on the shear modulus in the xy plane ($G_{c,xy}$), the shear modulus in the yz plane ($G_{c,yz}$) and the normal stiffness in the y-direction ($E_{c,y}$). Hence, longitudinal corrosion cracks would influence the lateral and torsional modes, as can be derived from Table 4. Moreover, as the crack depth of corrosion cracks is most often limited to the concrete cover, it is expected that the reduction of $G_{c,xy}$ mainly influences the torsional modes. This phenomenon is confirmed by the measurements presented in Fig. 7 and the discrete crack model in Fig. 9, which showed that mainly T1 and T2 are affected by longitudinal corrosion cracks.

On the other hand, perfectly transverse bending cracks influence the normal stiffness in x-direction ($E_{c,x}$), the shear modulus in the xy plane ($G_{c,xy}$) and the shear modulus in the xz plane ($G_{c,xz}$). As a result, the bending cracks and their combined decrease of $E_{c,x}$, $G_{c,xz}$ and $G_{c,xy}$ influence all modes (Table 4), as was also confirmed in the experimental results of Fig. 8 and the modelled results of Fig. 10.

5.2. Sensitivity of the modal characteristics on reduction of elastic moduli

Fig. 11 presents the relative changes in natural frequencies when the Young's moduli and shear moduli of the damaged concrete are reduced according to longitudinal or transverse cracking, when cracks are assumed to be bounded by the concrete cover. For longitudinal cracking, the Poisson's ratios $\nu_{c,xy}$ and $\nu_{c,yz}$ are reduced proportionally to the decrease in $E_{c,y}$, since the Eurocode proposes a reduced Poisson's, reaching up to 0, for cracked concrete [38]. The shear moduli ($G_{c,xy}$ and $G_{c,yz}$) experience a relatively lesser decrease, due to their dependence on both the Young's modulus and Poisson's ratio through Eq. (2). Likewise, $G_{c,xy}$ and $G_{c,xz}$ will decrease less than proportional to $E_{c,x}$, $\nu_{c,xy}$ and $\nu_{c,xz}$ when simulating transverse cracking.

The results in Fig. 11 show similar trends as the findings of the discrete crack models in Section 4.2. First, it can be seen that by decreasing $E_{c,y}$, $G_{c,xy}$ and $G_{c,yz}$, to simulate longitudinal cracking, mainly the natural frequencies of the torsional modes are affected. In addition, the frequencies of the lateral modes are slightly influenced while the frequency change of the bending modes can be neglected. The same results were found by the discrete crack model in Fig. 9.

Next, also transverse cracking is approximated well by reduction of $E_{c,x}$, $G_{c,xy}$ and $G_{c,xz}$. Fig. 11b shows that transverse cracking affects all modes, but the natural frequencies of the bending modes decrease most. The results of the discrete crack model in Fig. 10 and the experimental results presented in Fig. 8 illustrated similar findings, which validates the orthotropic smeared cracking approach. Nevertheless, it can be noticed that the torsional modes show a slightly larger decrease for the smeared cracking approach than for the discrete crack model.

6. Relation between geometrical crack parameters and elastic constants of the smeared crack model

Sections 4 and 5 described the discrete and smeared crack models and the influence of their respective crack parameters on the modal characteristics. The discrete crack models are able to link a certain crack pattern (i.e. crack width, amount of cracks and crack direction) to a decrease in natural frequencies, given selected values for the parameters of the weakened crack material. On the other hand, the smeared crack models link a decrease in stiffness to decreases in natural frequencies, yet cannot straightforwardly be linked to the geometrical crack parameters. In this section, the modal characteristics of the discrete crack models are compared to those of the smeared crack models, and both models are matched through RMSE in terms of absolute natural frequencies (Eq. (3)). This methodology allows to match crack patterns with decreases in stiffness. For example, a beam with 10 transverse cracks/m and a tensile strain of $\varepsilon_t = 0.01$ (Fig. 10b) shows similar decreases in natural frequencies as a beam with a 70% reduced $E_{c,x}$, $\nu_{c,xy}$ and $\nu_{c,xz}$ (Fig. 11b).

The proposed methodology is applied on many different crack patterns in order to obtain relations between crack parameters and stiffness reduction for lateral and transverse cracking. A total of nine different cracking zones are taken into account: 0 – 400 mm/0 – 800 mm/0 – 1200 mm/0 – 1600 mm/0 – 2000 mm/400 – 800 mm/400 – 1200 mm/400 – 1600 mm/800 – 1200 mm. Within these zones, 1, 2, 3, 4 or 5 cracks are modelled in longitudinal direction or 3, 5, 8, 11 or 13 cracks in transverse direction. For the longitudinal cracks, the total crack width over the beam width was taken equal to 0.05, 0.1, 0.2, 0.5, 1 or 1.5 mm. Similarly, the total crack width over the section length was taken equal to 0.05, 0.1, 0.2, 0.5, 1, 1.5, 2.5, 4 mm for transverse cracking. In conclusion, a total of 630 different crack patterns were simulated in DIANA to obtain the relations presented in Fig. 12. The average RMSE between the eight considered absolute frequencies of the discrete and smeared FE models for the longitudinal crack patterns (270 crack patterns) equals 0.25 Hz. When considering the bending, lateral and torsional modes separately, the errors equal: $RMSE_B = 0.08$ Hz, $RMSE_L = 0.23$ Hz and $RMSE_T = 0.35$ Hz. Meanwhile, the average RMSE for transverse cracking (360 crack patterns) equals 2.89 Hz ($RMSE_B = 3.04$ Hz, $RMSE_L = 0.61$ Hz and $RMSE_T = 4.19$ Hz). Taking into account that the considered frequencies range between 210 and 1160 Hz, the obtained RMSEs are quite low.

The differences in crack width and amount of cracks are reflected by the apparent tensile strain (ε_l and ε_t) and normalised amount of cracks (N_l and N_t) in Fig. 12. In addition, the varying locations of the cracked zones are reflected by the 95% CI around the mean result. Nevertheless, since the smeared cracking is modelled around the same area as the discrete cracks (Fig. 1), the influence of the crack location is small, as illustrated by the narrow CI. It should further be noted that these relations have specifically been developed for longitudinal corrosion cracks and transverse bending cracks at the bottom of RC beams, which are of most concern when detected on site. Nevertheless, it is important to recognise the potential of the developed methodology to derive similar relations for other types of cracks (e.g. shear cracks, shrinkage cracks, etc.), which allows for the investigation of diverse crack patterns and their corresponding impacts on the concrete stiffness.

Further, the developed relations are compared to the model of Coronelli and Gambarova [15] (Eq. (1)) in Fig. 12. In the evaluation of Eq. (1), a value of $K = 0.1$ is taken for medium-diameter ribbed rebars, the strain at peak compressive stress equals $\varepsilon_{co} = 0.2\%$ and $\varepsilon_1 = \varepsilon_l$ or $\varepsilon_1 = \varepsilon_t$. The value of f_c, as well as the relation between f_c^* and E_c were presented in Table 2. The model of Coronelli and Gambarova [15] results in significantly smaller reductions of the stiffness for the cracked beams, see Fig. 12. The discrepancy is most likely caused by the fundamental difference in stress states between the corroded RC beams and the RC panels which were used during calibration of the relation given by Eq. (1). Furthermore, the relation does not differentiate between the stiffness direction, in contrast to the orthotropic methodology developed in this research where for instance only $E_{c,y}$, $G_{c,xy}$ and $G_{c,yz}$ are reduced to simulate longitudinal cracking. In addition, Eq. (1) does not take into account the effect of the amount of cracks, which clearly alters the stiffness decrease. Finally, the relation between the concrete compressive strength (f_c) and stiffness (E_c) presented in Table 1 is developed for static stiffnesses and may not be directly applicable to dynamic stiffness assessments.

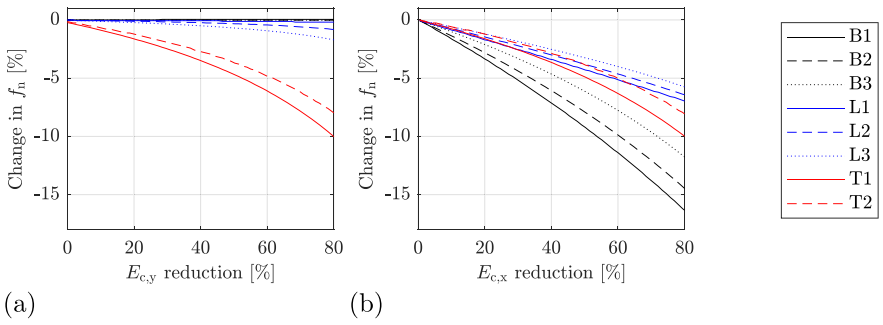

Fig. 11. Influence of the stiffness reduction caused by (a) longitudinal cracking ($E_{c,y}$, $G_{c,xy}$ and $G_{c,yz}$) and (b) the stiffness reduction caused by transverse cracking ($E_{c,x}$, $G_{c,xy}$ and $G_{c,xz}$) on the natural frequencies of a beam. The shear moduli G are derived from Eq. (2) by assuming a ν decreasing proportionally to E.

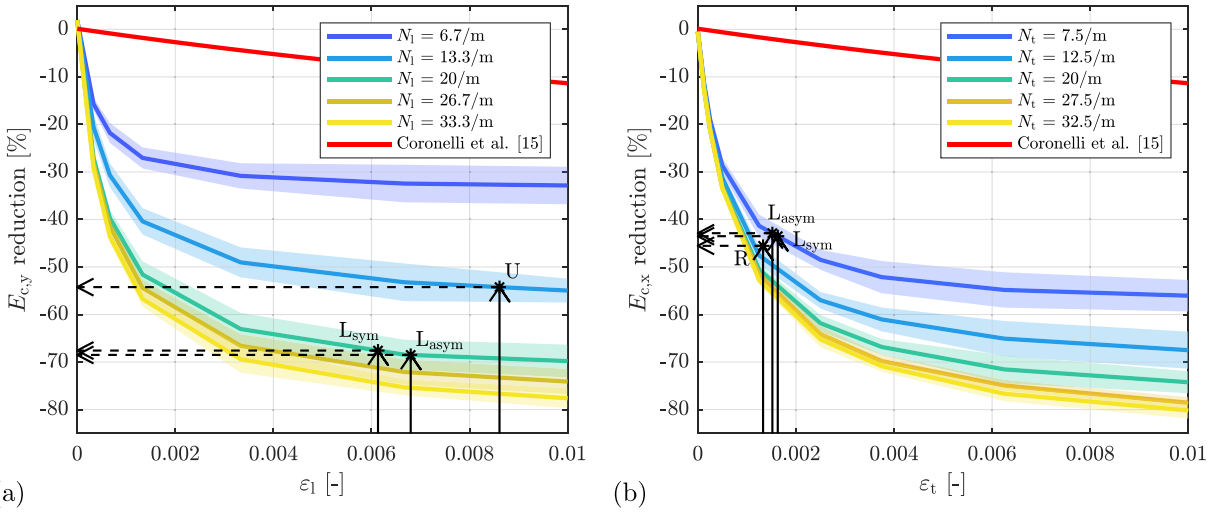

Fig. 12. Influence of the apparent tensile strain and number of cracks on the (a) stiffness reduction caused by longitudinal cracking ($E_{c,y}$, $G_{c,xy}$ and $G_{c,yz}$) and (b) stiffness reduction caused by transverse cracking ($E_{c,x}$, $G_{c,xy}$ and $G_{c,xz}$), with indication of the 95% CI. The shear moduli G are derived from Eq. (2) by assuming a ν decreasing proportionally to E. The asterisks indicate the parameters of the crack patterns at the end of the damage processes of the experimentally tested beams.

Next, the developed relations between crack parameters and stiffness decreases are verified by experimental measurements. Since ε_l, ε_t, N_l and N_t can be derived from crack measurements, the six crack patterns of the experimental tests discussed in Section 2 (Fig. 3) can be represented by a data point in the diagrams of Fig. 12 (illustrated by $*$ and arrows). Following the dotted arrows in Fig. 12, the corresponding decreases in stiffness parameters can be obtained. Smeared cracking FE models of the three beams with corrosion cracks (U, L_{sym}, L_{asym}) and the three beams with bending cracks (R, L_{sym}, L_{asym}) are developed based on the obtained stiffness reductions from Fig. 12. The resulting natural frequencies of the beam models are compared to experimental values in Fig. 13. After corrosion, the torsional modes are accurately predicted with RMSE = 0.53%. The measurements of T1 after corrosion, however, could not be reliably acquired for beams L_{sym} and L_{asym} and are therefore not included in the comparison. After four-point bending, the decreases in frequency of bending and lateral modes are slightly, yet consistently underestimated while the decrease in frequency of torsional modes is consistently overestimated by the smeared crack model. The resulting RMSE over all modes of the beams subjected to four-point bending equals RMSE = 2.97%, for relative changes in natural frequencies reaching up to −20%. The underestimation of the reduction of natural frequencies for vertical and lateral bending modes might be because the crack depth was assumed equal to the concrete cover in the development of the relations in Fig. 12. As illustrated in Fig. 3, the cracks after four-point bending reach up to 150 mm from the bottom of the beam. Nevertheless, since the modelled predictions are in the same order of magnitude as the measured results, and taking into account the many model and measurement uncertainties, it can be stated that the relations of Fig. 12 are able to predict the stiffness losses well.

Finally, to further validate the developed relations between crack properties and stiffness reduction, the proposed methodology is applied to three experimentally corroded and tested beams which were reported in the literature. Two beams with a length of 5 m were uniformly corroded in [45] to reach corrosion levels of 6.2% ($U_{6.2\%}$) and 5.2% ($U_{5.2\%}$). The apparent tensile strain ($\varepsilon_{l,6.2\%} = 0.0020/\varepsilon_{l,5.2\%} = 0.0012$) and amount of corrosion cracks ($N_{l,6.2\%} = 6.7/\text{m}/N_{l,5.2\%} = 6.7/\text{m}$) were derived from the reported crack patterns. Based on the relation in Fig. 12, a stiffness reduction of the cracked concrete cover of −28% and −26% is obtained, respectively. A third beam, reported in a previous paper by the authors [5], had a length of 3 m and was locally corroded (symmetrically) over a length of 400 mm to reach a corrosion level of 5.6% ($L_{5.6\%}$). The crack pattern of this beam resulted in $\varepsilon_{l,5.6\%} = 0.0076$ and $N_{l,5.6\%} = 13.3/\text{m}$, which leads to a stiffness reduction of −54%. The three beams were modelled in DIANA with the reported geometry and material properties, and cracked zones simulated according to the smeared crack method with stiffness reductions as derived here above. As previous results showed that the effect of longitudinal corrosion cracks on bending and lateral modes is negligible, Fig. 14 presents the simulated changes in natural frequencies of the torsional modes in comparison to the modal characteristics as reported in [5,45] after corrosion. It should be noted that the natural frequencies of mode T2 could not be captured accurately during measurements. Simulation of the natural frequency decrease of beam $U_{6.2\%}$ underestimates the measured values, potentially due to the influence of the support conditions during measurements [45]. Nevertheless, the results show an

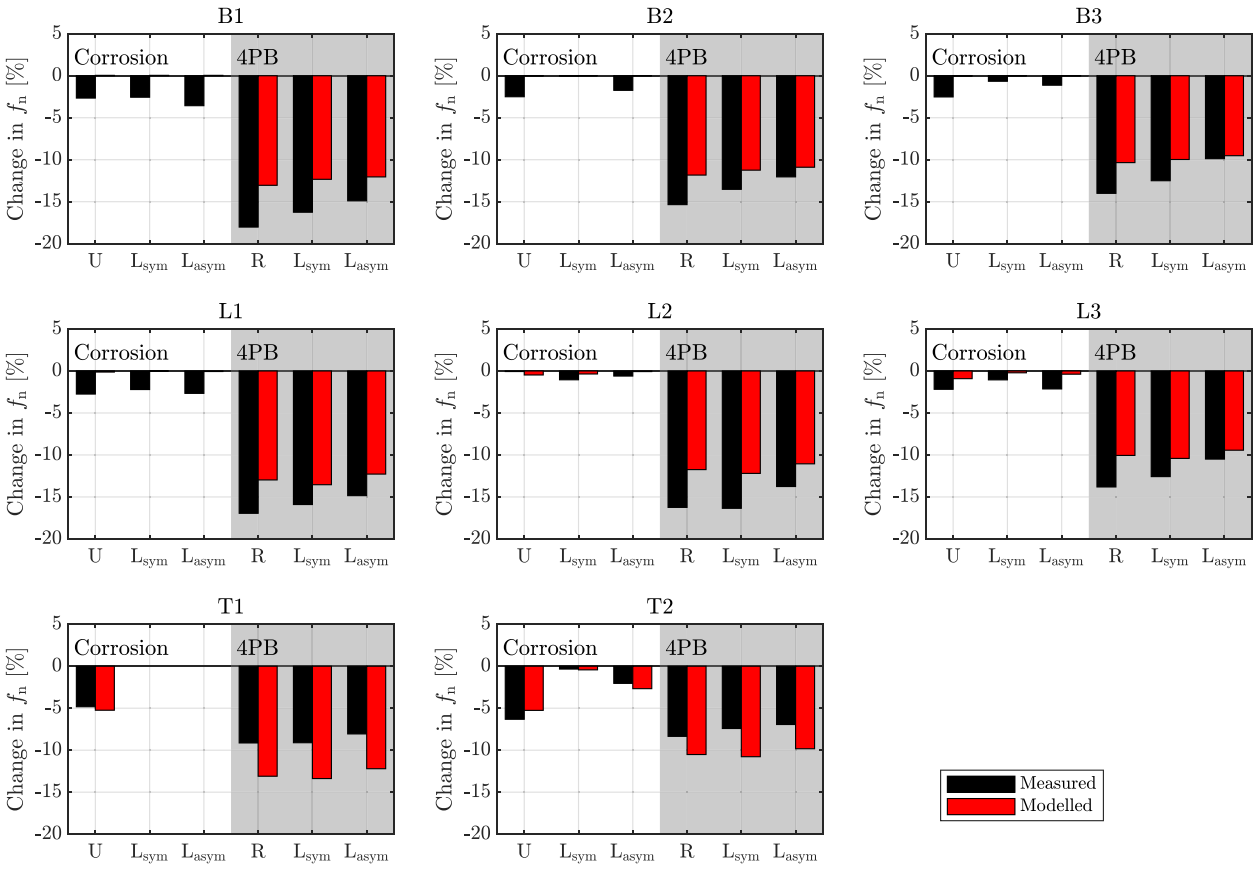

Fig. 13. Relative changes in measured natural frequencies after corrosion and four-point bending (4PB) of beams U, R, L_{sym} and L_{asym} compared to the modelled smeared crack results. Each graph represents a different mode.

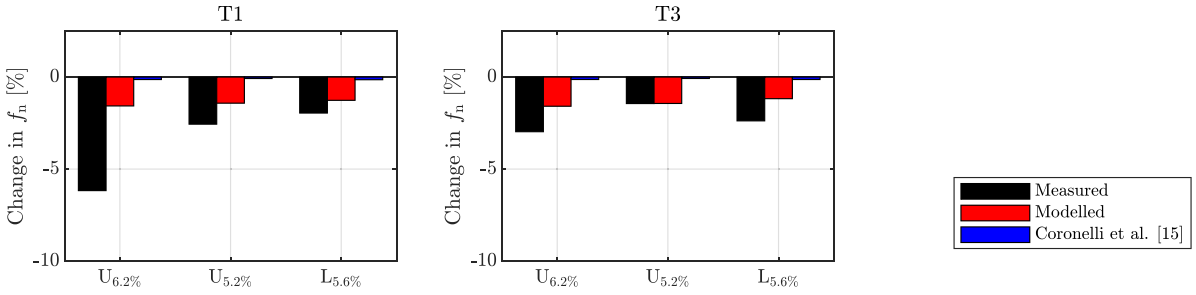

Fig. 14. Relative changes in measured natural frequencies of torsional modes after corrosion of beams $U_{6.2\%}$, $U_{5.2\%}$ and $L_{5.6\%}$, reported in the literature [5,45] (black), compared to the simulated smeared crack models obtained through the relations developed here (red) and the relation of Coronelli et al. [15] (blue). Each graph represents a different mode. (For interpretation of the references to colour in this figure legend, the reader is referred to the web version of this article.)

overall good agreement between measurements and simulated results, with an RMSE = 1.67%. In addition, also the relative changes in natural frequencies are shown when the relation of Coronelli and Gambarova [15] is used to determine the stiffness decrease. Comparison between the results clearly shows that the relation developed in this research is better suited for prediction of the decrease in dynamic structural stiffness due to corrosion cracking for RC beams with lengths between 2 – 5 m.

7. Conclusions

The main objective of this research was to develop a relation between the decrease in concrete stiffness and the observed crack pattern. This objective is accomplished by numerical simulation and validation with experimental testing. First, an FE model is established to represent undamaged RC beams, which is calibrated based on experimental dynamic tests. In order to accurately simulate the modal characteristics, it was found that the concrete's dynamic stiffness should be increased to 1.16 times the assumed static stiffness. Afterwards, discrete and smeared crack models are developed to obtain a relation between the crack properties and concrete stiffness decrease.

Discrete crack models are presented in which cracks are modelled through weakened elements with a Young's modulus of 20 MPa. Comparison of the discrete crack models with dynamic measurements of cracked RC beams shows that the developed weakened element approach simulates the modal characteristics of the damaged beams well. The RMSE between the relative decreases in natural frequency of measured and modelled results equals 1.94% for longitudinal corrosion-induced cracks and 2.83% for transverse bending cracks. Both the discrete crack model and experimental tests show that longitudinal corrosion cracks mainly influence torsional modes, while having a negligible effect on bending and lateral modes. Transverse cracking

has a more pronounced effect on the dynamic stiffness in comparison to longitudinal cracking, influencing bending, lateral and torsional modes. In addition, not only an increase in crack width reduces the dynamic stiffness, also the amount of cracks highly influences the modal characteristics.

Next, a smeared crack modelling approach is developed to link a local reduction of the effective Young's modulus and shear modulus in the cracked zone to the beam's modal characteristics. Since the crack direction has shown to greatly affect the modal characteristics, an orthotropic stiffness model is proposed to be able to differentiate between longitudinal and transverse cracking. Longitudinal cracking can be modelled through reduction of $E_{c,y}$, $G_{c,xy}$ and $G_{c,yz}$ while transverse cracks influence $E_{c,x}$, $G_{c,xy}$ and $G_{c,xz}$.

By coupling the natural frequencies of the beams simulated by discrete and smeared crack models, relations are developed between the crack properties and the dynamic stiffness reduction. These relations are able to predict the stiffness reduction of cracked RC beams based on parameters that can be obtained from visual inspection, such as the crack widths, amount of cracks and crack direction. Validation of the developed relations with experimental results shows that the stiffness losses and natural frequencies are generally well estimated with a model error of RMSE = 0.53% for longitudinal corrosion cracking and RMSE = 2.97% for transverse bending cracking. These errors are quite small, given that the relative decreases in natural frequencies during experimental testing reached up to −6% and −20% for corrosion cracking and transverse cracking, respectively. Further validation on corroded RC beams reported in the literature results in a model error of only RMSE = 1.67% for the simulation of natural frequency decreases. The presented research is therefore highly beneficial in predicting the stiffness loss of RC beams caused by cracking from rebar corrosion or bending, which are the most jeopardising cracking mechanisms on site.

Although application of the developed relation to various experimentally tested beams demonstrates its broad applicability, future research should investigate how the crack height and beam geometry influence the apparent concrete stiffness. In addition, the described methodology can be applied towards other frequently occurring crack types as well as environmental fluctuations to investigate their corresponding impacts on the structural stiffness.

CRediT authorship contribution statement

Eline Vandecruys: Writing – original draft, Visualization, Methodology, Investigation, Formal analysis, Conceptualization. **Max A.N. Hendriks:** Writing – review & editing, Supervision, Methodology, Conceptualization. **Menno van de Velde:** Writing – review & editing, Methodology, Investigation, Formal analysis, Conceptualization. **Geert Lombaert:** Writing – review & editing, Supervision, Methodology, Funding acquisition, Conceptualization. **Els Verstrynge:** Writing – review & editing, Supervision, Methodology, Funding acquisition, Conceptualization.

Declaration of competing interest

The authors declare that they have no known competing financial interests or personal relationships that could have appeared to influence the work reported in this paper.

Data availability

Data will be made available on request.

Acknowledgements

The authors would like to express their gratitude to Research Foundation Flanders, Belgium for their financial support (FWO PhD-grant no. 1SC1923N and V469923N).

References

[1] Li K, Li L. Crack-altered durability properties and performance of structural concretes. Cem Concr Res 2019;124:105811. http://dx.doi.org/10.1016/j.cemconres.2019.105811.
[2] François R, Laurens S, Deby F. Corrosion and its consequences for reinforced concrete structures. London, U.K.: ISTE Press Ltd; 2018.
[3] Fan W, Qiao P. Vibration-based damage identification methods: A review and comparative study. Struct Health Monit 2011;10(1):83–111. http://dx.doi.org/10.1177/1475921710365419.
[4] Carden EP, Fanning P. Vibration based condition monitoring: A review. Struct Health Monit 2004;3(4):355–77. http://dx.doi.org/10.1177/1475921704047500].
[5] Vandecruys E, Vereecken E, Anastasopoulos D, Verstrynge E, Caspeele R, Reynders E, et al. Challenges in assessing corrosion damage in reinforced concrete beams by vibration-based monitoring: literature analysis and experimental study. Struct Health Monit 2023;22(6):4233–51. http://dx.doi.org/10.1177/14759217231159321.
[6] Anastasopoulos D, De Roeck G, Reynders E. One-year operational modal analysis of a steel bridge from high-resolution macrostrain monitoring: Influence of temperature vs. retrofitting. Mech Syst Signal Process 2021;161(107951):1–21.
[7] Seo J, Hu JW, Lee J. Summary review of structural health monitoring applications for highway bridges. J Perform Constr Facil 2016;30(4):4015072. http://dx.doi.org/10.1061/(ASCE)CF.1943-5509.0000824.
[8] Brownjohn JMW, De Stefano A, Xu Y-L, Wenzel H, Aktan AE. Vibration-based monitoring of civil infrastructure: challenges and successes. J Civ Struct Health Monit 2011;1(3):79–95. http://dx.doi.org/10.1007/s13349-011-0009-5.
[9] Ortega NF, Robles SI. Assessment of residual life of concrete structures affected by reinforcement corrosion. HBRC J 2016;12(2):114–22. http://dx.doi.org/10.1016/j.hbrcj.2014.11.003.
[10] Fritzen CP, Jennewein D, Kiefer T. Damage detection based on model updating methods. Mech Syst Signal Process 1998;12(1):163–86. http://dx.doi.org/10.1006/mssp.1997.0139.
[11] Brownjohn JMW, Moyo P, Omenzetter P, Lu Y. Assessment of highway bridge upgrading by dynamic testing and finite-element model updating. J Bridge Eng 2003;8(3):162–72. http://dx.doi.org/10.1061/(ASCE)1084-0702(2003)8:3(162).
[12] Simoen E, De Roeck G, Lombaert G. Dealing with uncertainty in model updating for damage assessment: A review. Mech Syst Signal Process 2015;56–57:123–49. http://dx.doi.org/10.1016/j.ymssp.2014.11.001.
[13] Mosavi AA, Sedarat H, O'Connor SM, Emami-Naeini A, Lynch J. Calibrating a high-fidelity finite element model of a highway bridge using a multi-variable sensitivity-based optimisation approach. Struct Infrastruct Eng 2014;10(5):627–42. http://dx.doi.org/10.1080/15732479.2012.757793.
[14] Anastasopoulos D, De Roeck G, Reynders E. Influence of damage versus temperature on modal strains and neutral axis positions of beam-like structures. Mech Syst Signal Process 2019;134(106311):1–22. http://dx.doi.org/10.1016/j.ymssp.2019.106311.
[15] Coronelli D, Gambarova P. Structural assessment of corroded reinforced concrete beams: Modeling guidelines. J Struct Eng 2004;130(8):1214–24. http://dx.doi.org/10.1061/(ASCE)0733-9445(2004)130:8(1214).
[16] Vereecken E, Botte W, Lombaert G, Caspeele R. A Bayesian inference approach for the updating of spatially distributed corrosion model parameters based on heterogeneous measurement data. Struct Infrastruct Eng 2020. http://dx.doi.org/10.1080/15732479.2020.1833046.
[17] Bhargava K, Ghosh AK, Mori Y, Ramanujam S. Analytical model for time to cover cracking in RC structures due to rebar corrosion. Nucl Eng Des 2006;236(11):1123–39. http://dx.doi.org/10.1016/j.nucengdes.2005.10.011.
[18] Fahy C, Wheeler SJ, Gallipoli D, Grassl P. Corrosion induced cracking modelled by a coupled transport-structural approach. Cem Concr Res 2017;94:24–35. http://dx.doi.org/10.1016/j.cemconres.2017.01.007.
[19] Shayanfar MA, Barkhordari MA, Ghanooni-Bagha M. Effect of longitudinal rebar corrosion on the compressive strength reduction of concrete in reinforced concrete structure. Adv Struct Eng 2016;19(6):897–907. http://dx.doi.org/10.1177/1369433216630367.
[20] Musmar AM, Alhadi AN. Relationship between ultrasonic pulse velocity and standard concrete cube crushing strength. J Eng Sci 2008;36(1):51–9. http://dx.doi.org/10.21608/JESAUN.2008.115591.
[21] Vecchio FJ, Collins MP. The modified compression-field theory for reinforced concrete elements subjected to shear. ACI J 1986;83(2):219–31.
[22] Capozucca R. Detection of damage due to corrosion in prestressed RC beams by static and dynamic tests. Constr Build Mater 2008;22(5):738–46. http://dx.doi.org/10.1016/j.conbuildmat.2007.01.025.
[23] Vidal T, Castel A, François R. Corrosion process and structural performance of a 17 year old reinforced concrete beam stored in chloride environment. Cem Concr Res 2007;37(11):1551–61. http://dx.doi.org/10.1016/j.cemconres.2007.08.004.
[24] Fédération international du béton (fib). fib model code for concrete structures 2010. Ernst & Sohn, Wiley; 2013.
[25] Torres-Acosta AA, Fabela-Gallegos MJ, Muñoz-Noval A, Vázquez-Vega D, Hernandez-Jimenez JR, Martínez-Madrid M. Influence of corrosion on the structural stiffness of reinforced concrete beams. Corrosion 2004;60(9):862–72. http://dx.doi.org/10.5006/1.3287868.

[26] Castel A, Gilbert RI, Ranzi G. Instantaneous stiffness of cracked reinforced concrete including steel-concrete interface damage and long-term effects. J Struct Eng 2014;140(6). http://dx.doi.org/10.1061/(ASCE)ST.1943-541X.0000954.
[27] Miura T, Sato K, Nakamura H. The role of microcracking on the compressive strength and stiffness of cracked concrete with different crack widths and angles evaluated by DIC. Cem Concr Compos 2020;114:103768. http://dx.doi.org/10.1016/j.cemconcomp.2020.103768.
[28] Rots JG, Nauta P, Kuster G, Blaauwendraad J. Smeared crack approach and fracture localization in concrete. HERON 1985;30(1).
[29] Bazant ZP, Feng Bao LIN. Nonlocal smeared cracking model for concrete fracture. J Struct Eng 1988;144(11):2493–510.
[30] Tena-Colunga A, Abrams D. Estimating response of masonry structures with linear finite elements. In: Proceedings of the 5th North American masonry conference. 1990, p. 203–14.
[31] Menin R, Trautwein LM, Bittencourt TN. Smeared crack models for reinforced concrete beams by finite element method. Revista IBRACON Estruturas e Mater. 2009;2:166–200, 2.
[32] Gong F, Takahashi Y, Segawa I, Maekawa K. Mechanical properties of concrete with smeared cracking by alkali-silica reaction and freeze-thaw cycles. Cem Concr Compos 2020;111:103623. http://dx.doi.org/10.1016/j.cemconcomp.2020.103623.
[33] Blomfors M, G. Berrocal C, Lundgren K, Zandi K. Incorporation of pre-existing cracks in finite element analyses of reinforced concrete beams without transverse reinforcement. Eng Struct 2021;229:111601. http://dx.doi.org/10.1016/j.engstruct.2020.111601.
[34] Wang J, Shi Z, Nakano M. Strength degradation analysis of an aging RC girder bridge using FE crack analysis and simple capacity-evaluation equations. Eng Fract Mech 2013;108:209–21. http://dx.doi.org/10.1016/j.engfracmech.2013.04.011.
[35] Zhong J, Gardoni P, Rosowsky D. Stiffness degradation and time to cracking of cover concrete in reinforced concrete structures subject to corrosion. J Eng Mech 2010;136(2):209–19. http://dx.doi.org/10.1061/(ASCE)EM.1943-7889.0000074.
[36] Vandecruys E, van de Velde M, Reynders E, Lombaert G, Verstrynge E. Experimental study on acoustic emission sensing and vibration monitoring of corroding reinforced concrete beams. Eng Struct 2023;293:116553. http://dx.doi.org/10.1016/j.engstruct.2023.116553.
[37] van de Velde M, Vandecruys E, Verstrynge E, Reynders E, Lombaert G. Vibration monitoring and acoustic emission sensing during progressive load tests of corroded reinforced concrete beams. Eng Struct 2024;306:117851. http://dx.doi.org/10.1016/j.engstruct.2024.117851.
[38] European Committee for Standardization. Eurocode 2: Design of Concrete Structures - Part 1-1: General Rules and Rules for Buildings (EN 1992-1-1). 2005.
[39] Lim JC, Ozbakkaloglu T. Stress–strain model for normal- and light-weight concretes under uniaxial and triaxial compression. Comput Chem Eng 2014;71:492–509. http://dx.doi.org/10.1016/j.conbuildmat.2014.08.050.
[40] Tena-Colunga A. Aspects to consider in the assessment of effective stiffness for reinforced concrete beams. J Archit Eng 2021;27(1). http://dx.doi.org/10.1061/(ASCE)AE.1943-5568.0000451.
[41] European Committee for Standardization. EN 12390-3: Testing hardened concrete - Part 3: Compressive strength of test specimens. 2019.
[42] European Committee for Standardization. EN 12390-7: Testing hardened concrete - Part 7: Density of hardened concrete. 2019.
[43] European Committee for Standardization. Eurocode 3: Design of steel structures - Part 1-1: General rules and rules for buildings (EN 1993-1-1). 2005.
[44] Musiał M, Trapko T, Grosel J. Static and dynamic stiffness of reinforced concrete beams strengthened with externally bonded CFRP strips. Materials 2021;14(4):1–22. http://dx.doi.org/10.3390/ma14040910.
[45] Vereecken E. Applied Bayesian pre-posterior and life-cycle cost analysis for determining and optimizing the value of structural health monitoring for concrete structures (Ph.D. thesis), Ghent University; 2022.